SCALING WEARABLE FOUNDATION MODELS

Anonymous authors
Paper under double-blind review

ABSTRACT

Wearable sensors have become ubiquitous thanks to a variety of health tracking features. The resulting continuous and longitudinal measurements from everyday life generate large volumes of data; however, making sense of these observations for scientific and actionable insights is non-trivial. Inspired by the empirical success of generative modeling, where large neural networks learn powerful representations from vast amounts of text, image, video, or audio data, we investigate the scaling properties of sensor foundation models across compute, data, and model size. Using a dataset of up to 40 million hours of in-situ heart rate, heart rate variability, electrodermal activity, accelerometer, skin temperature, and altimeter per-minute data from over 165,000 people, we create LSM, a multimodal foundation model built on the largest wearable-signals dataset with the most extensive range of sensor modalities to date. Our results establish the scaling laws of LSM for tasks such as imputation, interpolation and extrapolation, both across time and sensor modalities. Moreover, we highlight how LSM enables sample-efficient downstream learning for tasks like exercise and activity recognition.

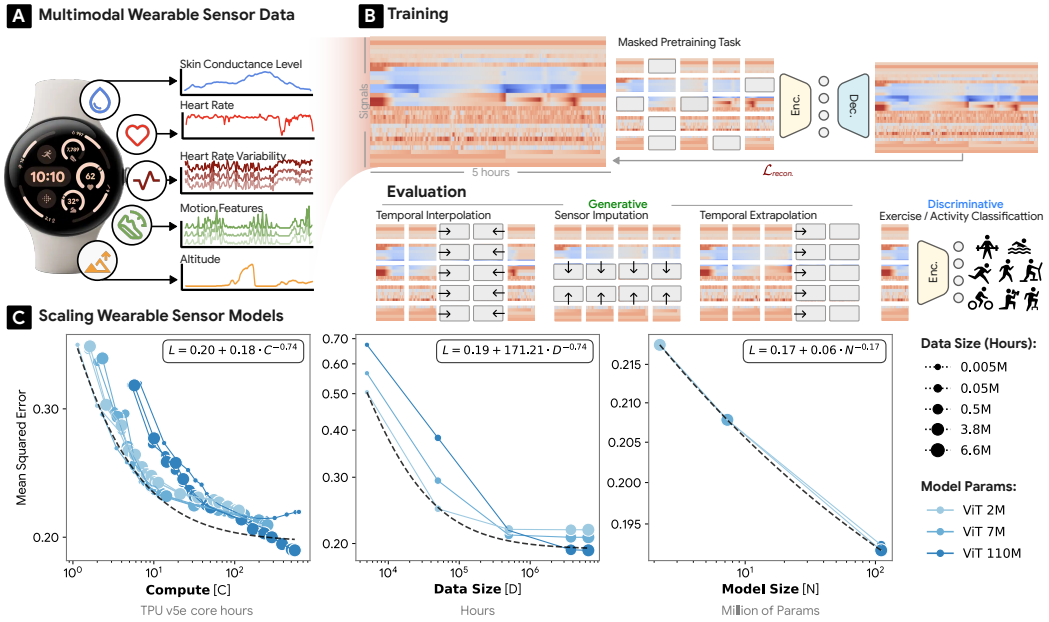

Figure 1: **Scaling foundation models on wearable data.** Making sense of physiological and behavioral signals derived from wearables is challenging. **(A)** We present a systematic scaling analysis of sensor models using up to 40 million hours of multimodal data from over 165,000 people. **(B)** Using a random masking pretext task, we evaluate on tasks of imputation, forecasting, and downstream classification. **(C)** Experiments show scaling compute, data, and model size are all effective. Scaling is shown on the random imputation task.

1 INTRODUCTION

Wearable devices that monitor physiological and behavioral signals have become ubiquitous. Increasing evidence suggests that these devices can significantly contribute to promoting healthy be-

haviors (Ringeval et al., 2020), detecting diseases (Yang et al., 2022), and enhancing the design and implementation of treatments (Munos et al., 2016). These devices generate large volumes of continuous, longitudinal, and multimodal data. However such wearable time series data can be difficult for consumers and experts to interpret. To this end algorithms have been developed to translate time series sensor data into human-readable representations, such as step counts and heart rates.

Historically, algorithms for wearable sensors have relied on supervised, discriminative models designed to detect specific events or activities (Lubitz et al., 2022). This approach, however, faces several significant limitations. First, the *limited volume and severe data imbalance* of labeled events results in large amounts of valuable *unlabeled* data being left unused. Second, supervised models are typically trained for *a single task* (e.g., classification), producing representations that may not generalize well to other tasks. Third, training data is often collected from *small study populations* (usually involving only tens or hundreds of participants), leading to a lack of diversity in the data.

Self-supervised learning (SSL) using generic pretext tasks (Noroozi et al., 2017; Caron et al., 2018; Yang et al., 2023) can yield versatile representations that are useful for a wide range of downstream applications. SSL allows for the use of a much larger proportion of available data without being restricted to labeled data regions (e.g., a limited number of subjects who self-report labels for exercises/activities). These advantages have motivated efforts to apply similar training strategies to build models from large volumes of unlabeled wearable data (Adaimi et al., 2024; Thapa et al., 2024; Yuan et al., 2024; Abbaspourazad et al., 2023) (see Table 1 for a summary).

Building on this, the empirical and theoretical success of scaling laws in neural models (Kaplan et al., 2020; Bahri et al., 2024) suggests that model performance improves predictably as compute, data, and model parameters increase. These findings raise a critical research question: **Do scaling laws apply to models trained on wearable sensor data?** We aim to investigate whether the principles that drive the scaling of neural networks in domains like language and vision also extend to large-scale, multimodal wearable sensor data. Understanding how scaling manifests in this context could not only shape model design but also enhance generalization across diverse tasks and datasets.

In this paper, we present the results of our scaling experiments on the largest and the most diverse wearable dataset published to date, comprising 40 million hours of multimodal sensor data from over 165,000 users (Fig. 1). Leveraging these data, we train a foundation model, referred to as the **Large Sensor Model** (`LSM`), which is designed to capture generalizable representations across diverse populations, wearable sensor modalities, and downstream tasks. We demonstrate the scaling properties of `LSM` with respect to compute, data size, and model parameters, leading to substantial performance gains on generative imputation, interpolation and extrapolation as well as downstream discriminative tasks. Our contributions can be summarized as follows:

- Implementation of the largest study to date on the scaling behavior of sensor foundation models, encompassing 40 millions hours, over 165,000 users and multiple sensor modalities, including accelerometer, photoplethysmography (PPG), electrodermal activity (EDA), skin temperature, and altimeter signals.
- Identification of key strategies for training large-scale sensor foundation models (`LSM`), and the `LSM`'s scaling properties with respect to compute, data size, and model parameters.
- Demonstration of the model's ability to impute, interpolate, and extrapolate across temporal and sensor modalities, with a particular focus on generalization to unseen users.
- Verification that learned representations can be applied to downstream classification tasks, such as exercise and activity recognition, using ecologically valid, user-annotated events.

2 Related Work

Sensor Foundation Models. Recent advances have demonstrated improved accuracy, robustness, and generalizability of models for sensor data by utilizing self-supervised pretraining on large-scale corpora of behavioral and physiological signals (Yuan et al., 2024; Thapa et al., 2024; Merrill & Althoff, 2023). Existing sensor foundation models primarily leverage contrastive learning, creating positive and negative data pairs (Yuan et al., 2024; Thapa et al., 2024; Abbaspourazad et al., 2023). Yuan et al. (2024) employ time domain augmentations (e.g., reversal, warping, permutation) to formulate the SSL task for motion data. Abbaspourazad et al. (2023) adopt a similar strategy, incorporating Gaussian noise, time and magnitude warping, and channel swapping. Thapa et al.

Table 1: **Comparisons of studies on wearable sensor foundation models.**

Study	# People (000s)	# Hours (000s)	Sensors						Generative
			ECG	PPG	ACC	SCL	TMP	ALT	
Adaimi et al. (2024)	0.05	0.20	✗	✗	✓	✗	✗	✗	✓
Abbaspourazad et al. (2023)	141	400	✓	✓	✗	✗	✗	✗	✗
Yuan et al. (2024)	100	15,700	✗	✗	✓	✗	✗	✗	✗
LSM **(Ours)**	**165**	**40,000**	✗	✓	✓	✓	✓	✓	✓

ECG: Electrocardiography, PPG: Photoplethysmography, ACC: Accelerometer, SCL: Skin Conductance Level, TMP: Skin Temperature, ALT: Altimeter

(2024) generate data pairs using different sensory modalities. In contrast, we focus on *masked input modeling* due to the generative capabilities that it offers and explore its properties when scaling compute, data size, and model size. Compared to prior work we consider more sensor inputs, a larger data sample, and systematically investigate scaling laws (see Table 1). We also present contrastive baselines (Assran et al., 2022; Chen et al., 2020) where applicable.

Time-Series Foundation Models. Wearable sensor data typically takes the form of multivariate time series. Foundation models for time-series signals have been trained and evaluated on data from domains such as energy use, transportation, finance, and climate. TimeGPT (Garza & Mergenthaler-Canseco, 2023) and Lag-Llama (Rasul et al., 2023) represented early versions of pretrained models for predicting time-series signals. Families of models for general-purpose time series analysis emphasize common properties present in many signals, even those from different sources (Goswami et al., 2024). Recent efforts explore different model architectures (Das et al., 2023) and scaling multiple data sources (Ansari et al., 2024), examing how language models can perform zero-shot reasoning (Liu et al., 2023; Merrill et al., 2024). Yet, time series from different domains can exhibit considerably different properties. Drawing inspiration from prior work, we focus on the analysis of *sensory* time-series data, exploring scaling behavior, and interrogating whether they are consistent with other domains or show unique properties.

Scaling Laws in Deep Learning. The scaling of computational resources, data volume, and model size has driven remarkable advancements in deep learning (Zhai et al., 2022; Kaplan et al., 2020; Xie et al., 2023). Recent investigations indicate that testing loss follows a power law relationship with each of these three resources when the other two are held constant (Kaplan et al., 2020). Power law behavior has been observed across various domains, including large language models (Kaplan et al., 2020), large vision models (Zhai et al., 2022), transfer learning (Hestness et al., 2017), and multimodal models (Aghajanyan et al., 2023). In this work, we take a step further and investigate the scaling behavior of training foundation models for multimodal *wearable sensor* data.

3 Data for Wearable Foundation Models

3.1 Sensor Data and Processing

Fitbit Sense 2 and Pixel Watch 2 have four *sensors* of highest relevance to this work: PPG, accelerometer, skin conductance, and altimeter/pressure sensors. From these input signals we compute a set of 26 *signals* (features), as described in Table 18 of Appendix G. Raw sensor data is not stored at this scale as it would impact the battery life and memory on the device. Thus, we focus on one-minute resolution signals.

SCL **Skin Conductance.** The EDA sensor is used to infer sympathetic arousal via changes in micro-sweat levels, a physiological response to stress. Two electrodes on the back of the device measure changes in skin conductance level (SCL), which varies with skin moisture levels. SCL data is sampled at 200 Hz, downsampled to 25 Hz via a boxcar filter, and smoothed with a 5-minute

Table 2: **Details of the datasets.** Summary of the demographic composition of our pretraining set and class distribution of our downstream set samples.

(a) **Demographics of the pretraining set.**

	Category	# People	%
Sex	Female	110,780	67.0%
	Male	53,895	32.6%
	Not Specified	415	0.3%
Age	18-39	55,653	33.7%
	40-59	75,627	45.8%
	60-79	32,251	19.5%
	$\geq$80	1,548	0.9%
BMI	Healthy ($<$25)	57,015	34.5%
	Overweight (25-30)	52,950	32.0%
	Obese ($\geq$30)	54,727	33.1%
	Not Specified	575	0.3%
	Total	165,090	100%

(b) **Class sample distribution of the downstream set.**

Class	# Training	# Testing
Exercise	3,272	671
Non-Exercise	6,195	1,329
Total	9,467	2,000
Biking	1,191	412
Elliptical	152	49
High Intensity Training	332	104
Strength Training	229	425
Swimming	2,332	441
Running	1,860	315
Walking	6,887	1,301
Weightlifting	669	98
Total	14,372	3,262

median low-pass filter (McDuff et al., 2024). Per-minute tonic SCL slope and magnitude are then calculated. Due to the nature of the sensing mode operation, SCL data is only collected during non-exercise wake-periods.

TMP **Skin Temperature.** A temperature sensor located near the wrist-facing surface of the device takes measurement every 10 seconds. Per-minute slope and magnitude values are calculated via linear regression. Skin temperature signals are available whenever EDA signals are available.

PPG **Photoplethysmography.** A validated algorithm (Nissen et al., 2022) is used to extract heart rate (HR) once per second from PPG. The per-minute HR data was calculated by taking the mean of the interpolated, per-second data across non-overlapping one-minute windows. An on-device peak detection algorithm identified PPG-based R-wave peaks from which RR intervals were calculated. RR intervals are susceptible to noise from multiple sources, including movement, electronic noise, and missed heartbeats. To account for noise, outliers were removed from each sliding 5-minute window using the median-filter based approach (Natarajan et al., 2020). The percentage of each 5-minute window with valid RR intervals are calculated and referred to as "heart rate variability (HRV) percent good". Nine standard HRV metrics (Shaffer & Ginsberg, 2017) are calculated every minute over a sliding 5-minute window: RR mean, RR median, RR 20th percentile, RR 80th percentile, RR Shannon Entropy, RR differences Shannon Entropy, standard deviation of RR, root mean squared difference of RR intervals, and percentage of RR intervals greater than 30ms (PNN30).

ACC **Accelerometer.** Ten signals are extracted from the 3-axis accelerometer: Jerk, steps, accelerometer log energy and energy ratio, covariance, number of zero crossings and standard deviation. These signals are extracted by converting the 3-axis accelerometer to root mean squared magnitude (1D), and applying a high-pass filter (HPF) to the remove the DC component. In parallel, the 3-axis accelerometer signal is put through a second-order band-pass filter (BPF) and the principal component of the filtered 3-axis signal covariance matrix is calculated and updated every 25 seconds. Jerk is a measure based on the time-derivative of the acceleration calculated from the principal component. It is the logarithm of the ratio of the absolute of the t=1 autocorrelation lag over the t=0 autocorrelation lag. Steps is a per-minute count of steps taken calculated based on a machine learned classifier. Log energy is the logarithm of the sum of the squared HPF signal over the window. Log energy ratio is the logarithm of the ratio of energy computed from principal-component over the magnitude of the HPF signal. Zero-crossing count is the number of crossings in the principal component and standard deviation is the calculated from the sample window. Kurtosis is calculated from the BPF signal. Each of these features is originally computed every 51 seconds and then resampled to a minutely resolution. Sleep coefficient is calculated as the sum of the 3-axes max-min range and binned into 16 log scaled bins before being input into a machine learned classifier to predict wake vs. sleep probability.

ALT **Altimeter.** The standard deviation of the altimeter (pressure sensor) measurements.

All sensor signals were globally normalized (z-score) to remove differences in magnitude due to different units of measurement. As the masked autoencoder cannot process missing data, we imputed minutes that had missing values. Within each 300-minute window, missing data between valid data points was linearly interpolated, and leading missing minutes were backfilled.

3.2 Building A Large Scale Pretraining Sensor Dataset

To build the large dataset for our experiments we sampled wearable data from 165,090 subjects during the period January 1st 2023 to July 2nd 2024. The subjects wore Fitbit Sense 2 or Google Pixel Watch 2 devices and consented for their data to be used for research and development of new health and wellness products and services. We sub-selected from people wearing one of these devices as older device generations included fewer sensors. The subjects were asked for self-reported sex, age and weight. Table 2(a) summarizes the characteristics of the pretraining data. All data were de-identified and not linked with any other information. To create a dataset that maximized the number of subjects we randomly sampled 10 5-hour windows of data from each subject, for a total of 8 million hours (6.6 million pretrain hours). We further explore the extremes of data scaling by experimenting with a subject-imbalanced 40 million hour pretraining dataset (see Appendix C.1). Note that this dataset is comprised of wearable data from daily-living, including diverse timestamps and a range of life events, and thus is not biased toward specific events or activities.

The dataset was split 80-20 based on subjects into train-test splits (132072 subjects in training, 33018 subjects in testing) as described in Table 2(a). We then created several "slices" of the training set to conduct the scaling experiment. The test set remains identical throughout all experiments. In the "sample-scaling" experiments we shuffled the training data and took N samples per experiment. In the "subject-scaling" experiments we grouped the training data by subject identifier and took all samples from N subjects per experiment.

4 Sensor Modeling Tasks

4.1 Generative Tasks

We posit that defining generative tasks in the training of wearable sensor models may not only result in learned representations that are useful for downstream classification tasks, but also produce models that can impute missing or incomplete data (interpolate) and extrapolate future sensor values (forecast). To train the model and to test these capabilities we define several tasks (see Fig. 2).

Random Imputation. Our primary pretext task involves removing patches randomly from the input sample across the time-axis and signal-axis. During training this requires the model to infer missing values and make predictions based on partial input.

Temporal Interpolation. Sensor inputs can be missing for a number of reasons. Devices need to be removed from the wrist for charging, and certain sensors might be turned off for periods to save on battery life (McDuff et al., 2024). Interpolation of sensor data is an important and necessary step for many algorithms (see Fig. 2). In this task we test the model's ability to fill gaps in the data where all sensor data is missing for a period of time, usually between two observations.

Sensor Imputation. Sensor imputation refers to the process of inferring a subset of partially missing sensor-streams, from other continuously online sensing modalities. By leveraging correlations between different physiological signals, sensor imputation ensures that insights can be derived even when some sensor modalities are absent, enhancing the overall versatility and capabilities of multi-sensor systems. Under the constraints of hardware limitations (battery, wireless connectivity, etc.), sensor imputation can enable the delivery of more realistic metrics to the user (e.g., step count, average resting heart rate) even if when sensors are not continuously online.

Temporal Extrapolation (Forecasting). A more challenging task than interpolation is extrapolation of sensor values forward in time. Temporal extrapolation involves predicting future sensor measurements. The ability to anticipate future physiological states based on current and historical data has applications in areas such as health interventions, where extrapolation can be used to schedule recovery times, detect early signs of fatigue, predict wake-up times, and detect anoma-

Figure 2: **Generative LSM tasks and pretraining.** We define four distinct generative tasks: random imputation, temporal interpolation, signal/sensor imputation, and temporal extrapolation (forecasting). Random imputation was empirically chosen as the pretraining task.

lies. Accurate signal extrapolation is a key task that can empower wearable devices to provide more just-in-time, proactive, and personalized health recommendations.

4.2 Discriminative Tasks

Discriminative tasks focus on classifying or identifying specific activities, states, or conditions based on sensor data. These tasks are essential for translating raw sensor inputs into actionable, personalized, and relevant feedback. The corresponding datasets are split 80-20 into user-stratified train-test splits unless otherwise specified. Two exemplary tasks are considered here. Additional discriminative tasks (sex, binned age, and subject dependent mood) and results can be found in Appendix C.7.

Activity Recognition. Activity recognition is the process of classifying different user activities such as biking, running, or walking, based on the patterns detected in sensor data. This allows wearable devices to monitor daily routines accurately, providing insights into fitness levels, activity trends, and overall health. Effective activity recognition enables applications like fitness tracking, lifestyle monitoring, and personalized coaching. Our dataset includes eight user-labeled activities: *Biking*, *Elliptical*, *High-Intensity Interval Training (HIIT)*, *Strength Training*, *Swimming*, *Running*, *Walking*, and *Weightlifting*. The activity event labels are self-reported by users post hoc.

Exercise Detection. Exercise detection identifies when a user is exercising, enabling real-time feedback and performance tracking. This task involves recognizing exercise events from continuous sensor data, allowing devices to log workout sessions, track progress, and provide personalized recommendations. Additionally, detecting exercise unlocks related experiences, such as identifying exercise types, marking session start times, or tracking post-exercise feedback. We developed a dataset with windows of user-labeled exercise and non-exercise events (see Table 2(b)). The exercise event labels are based on self-reported activity labels.

5 Experiments & Results

5.1 Training Procedures

We pretrain our wearable foundation models on a diverse collection of multimodal sensor data. Each sample is processed as a two-dimensional matrix of 26 signals by 300 minutes (see Fig. 2). Our primary pretraining objective is to optimize the masked signal reconstruction loss (i.e., mean squared

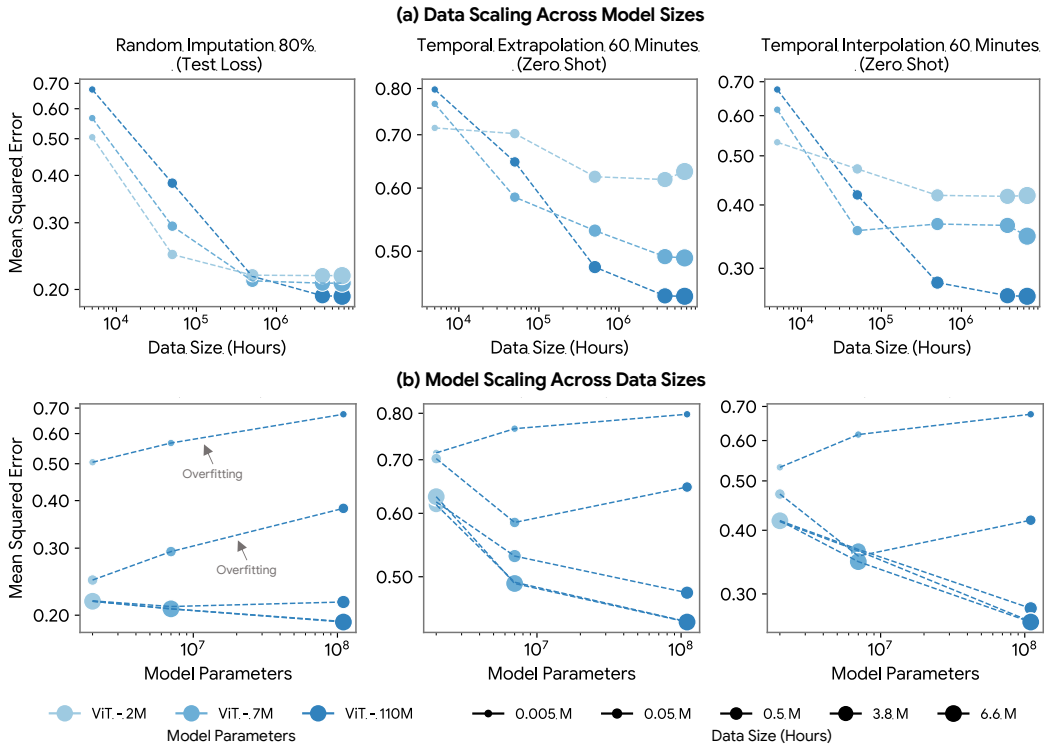

Figure 3: **Scaling performance of LSM.** We show performance on *generative tasks* across varying data and model sizes. LSM begins to saturate at approximately 10^7 hours of data. The effects of scaling are more pronounced in imputation, interpolation, and extrapolation tasks. Results indicate that as model size increases, significantly larger data volumes are required to prevent overfitting.

error), averaged over randomly masked patches from the input matrix (He et al., 2022). The primary performance metric is the mean squared error on the held-out test set, evaluated across all the normalized signals. We employ a masked autoencoder (MAE) due to it's ability to handle multitarget generative tasks like forecasting and interpolation, and discriminative tasks such as activity recognition, unlike traditional time-series models that focus on single-target prediction (Ansari et al., 2024). Furthermore, MAE gracefully handles missingness which is inherent in wearable data. MAE has proven effective in pretraining and scalable learning across domains (Huang et al., 2022; Xie et al., 2023), which aligns with our focus on establishing scaling laws in the wearable data domain.

We pretrain our models on Google v5e TPUs with a total batch size of 4096 across 50,000 training steps. The training process uses the AdamW optimizer with a base learning rate of $5e-3$ and weight decay set to $1e-4$. A linear warm-up schedule is applied for the first 2,500 steps, followed by a cosine learning rate decay to zero. All pretraining experiments use an 0.8 masking ratio (masking out random patches that cover 80% of the total input signals). Additional details on implementation and hyperparameters can be found in Appendix E.

5.2 Results & Discussion

Do scaling laws apply to wearable data? We present the Pareto front of the reconstruction loss and downstream performance as a function of *compute scaling* (see Fig. 1). The front highlights the models with optimal compute allocation across model size, data size and training duration. Over multiple orders of magnitude of compute, the relationship between compute and performance follows a power-law ($L = aC^b$), resulting in a nearly linear trend on the log-log plot. However, we observe a saturation effect at the upper end of the compute spectrum, where the largest models do not asymptotically approach zero error. This behavior has also been observed for scaling language models (Henighan et al., 2020) and vision transformers (Zhai et al., 2022); therefore, we add an additive constant c to model this saturation effect: $L = aC^b + c$.

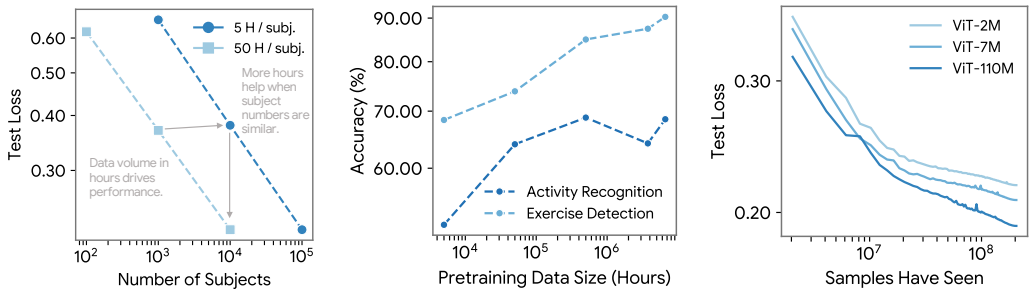

(a) Scaling Subjects (b) Scaling on Downstream Tasks (c) Learning Efficiency

Figure 4: **Analysis on scaling** `LSM`**. (a)** Total number of hours is more important than total number of subjects. **(b)** Data scaling on discriminative tasks with ViT-110M. **(c)** Larger models are more sample efficient.

We illustrate *data scaling* across various model sizes (Fig. 3(a)). Performance improves monotonically to approximately 10^5 data hours, beyond which the rate of improvement diminishes, particularly around 10^7 hours. We validated that scaling beyond 10^7 hours yields minimal benefits by training with 40 million hours (see Appendix C.1). Consequently, results in Table 3 are pretrained with 6.6 million hours of data. Larger models, especially the ViT-110M, continue to benefit from data scaling, showing substantial gains when training on over 1 million hours of data. These observations underscore the large data requirements needed to fully exploit the capacity of larger models, which are far greater than those required by smaller models. A similar trend is observed in discriminative tasks (Fig. 4(b)). We further note that these trends are based on minutely aggregated wearable data; raw sensor signals are traditionally collected at substantially higher sampling frequencies and it is possible that feature extraction on more fine-grained sensor data may require even larger models.

Model scaling results as a function of data size demonstrate that as both model size and dataset size are scaled, sufficient data is essential to prevent overfitting (Fig. 3(b)). Models trained on smaller datasets exhibit limited generalization capacity, whereas scaling up to 10^8 parameters results in significant gains in test loss and generative zero-shot performance. These findings highlight the need to align model size with adequate data to fully leverage the model's representational power. Our experiments also show larger models are more sample efficient as illustrated in Fig. 4(c).

By scaling compute, data, and model size together, `LSM` achieves improvements of 16% to 23% in temporal interpolation MAE and 20% to 21% in extrapolation MAE across five time durations as compared to the best baseline method (Table 3(a)). Additionally, `LSM` outperforms baselines in exercise detection and 8-class activity recognition over the supervised baseline by 27% / 29% in accuracy and 57% / 54% in mAP, as detailed in Table 3(c). Our baseline approaches are commonly used in existing sensor algorithms (Gershon et al., 2016; van Rossum et al., 2023). More scaling results can be found in Appendix C.

Is scaling subjects or wearable data hours per subject more helpful? As shown in Fig. 4(a), when training using the same total number of wearable signal hours, reducing the number of subjects (but drawing more hours per subject) can yield similar performance. This suggests that total number of hours rather than number of subjects drives gains. One possible hypothesis to explain this effect is that the diversity of activities per subject (as reflected by the increase in hours per subject) plays a crucial role. Alternatively, subject diversity may become more important when learning representations if we scale up the data sample size from 5 hours (e.g., 7 days vs. 5 hours). As each subject has a finite number of hours, to maximize model generalization, it is important to scale both the number of subjects and the wearable data hours per subject simultaneously. While temporal data is crucial for capturing intra-subject variability, increasing the number of subjects introduces valuable inter-subject diversity. Therefore, scaling both dimensions—subjects and hours—together is essential to fully leverage the model's capacity and improve performance across tasks.

Can wearable foundation models impute the past and predict the future? As shown in Fig. 3, scaling laws apply to all imputation, interpolation, and extrapolation tasks, with larger models and more data resulting in improved performance. The utility of `LSM` is further emphasized in Table 3(a). However, despite these quantitative gains, the qualitative results in Fig. 11 of Appendix C.6 reveal

Table 3: **Comparisons of LSM and competing methods on generative and discriminative tasks.**

(a) **Generative Task Results**

Task + Method	**Error (MAE / MSE)**				
Temporal Interpolation	**10 mins**	**20 mins**	**30 mins**	**60 mins**	**120 mins**
MEAN	0.36 / 0.42	0.36 / 0.43	0.37 / 0.44	0.38 / 0.46	0.39 / 0.49
MICE	0.36 / 0.42	0.36 / 0.43	0.37 / 0.43	0.38 / 0.45	0.39 / 0.48
NEAREST NEIGHBOR	0.21 / 0.29	0.26 / 0.37	0.28 / 0.42	0.33 / 0.51	0.38 / 0.62
LINEAR INTERP.	0.19 / 0.23	0.23 / 0.30	0.26 / 0.34	0.30 / 0.42	0.36 / 0.51
LSM (MAE)	**0.16 / 0.14**	**0.19 / 0.18**	**0.20 / 0.21**	**0.24 / 0.26**	**0.29 / 0.33**
GAINS OVER INTERP.	**+16% / 39%**	**+17% / 40%**	**+23% / 38%**	**+20% / 38%**	**+19% / 33%**
Temporal Extrapolation	**10 mins**	**20 mins**	**30 mins**	**60 mins**	**120 mins**
MEAN	0.48 / 0.66	0.48 / 0.65	0.47 / 0.65	0.47 / 0.64	0.45 / 0.64
MICE	0.48 / 0.66	0.48 / 0.66	0.47 / 0.65	0.47 / 0.65	0.45 / 0.64
NEAREST NEIGHBOR	0.35 / 0.52	0.40 / 0.62	0.43 / 0.68	0.47 / 0.76	0.48 / 0.81
LINEAR INTERP.	0.35 / 0.52	0.40 / 0.62	0.43 / 0.68	0.47 / 0.76	0.48 / 0.81
LSM (MAE)	**0.28 / 0.31**	**0.32 / 0.37**	**0.34 / 0.40**	**0.37 / 0.44**	**0.38 / 0.47**
GAINS OVER INTERP.	**+20% / 40%**	**+20% / 40%**	**+21% / 23%**	**+21% / 31%**	**+21% / 27%**
Sensor Imputation	**10 mins**	**20 mins**	**30 mins**	**60 mins**	**120 mins**
MEAN	0.36 / 0.42	0.36 / 0.43	0.37 / 0.43	0.38 / 0.45	0.39 / 0.49
MICE	0.30 / 0.33	0.30 / 0.36	0.31 / 0.38	0.33 / 0.46	0.37 / 0.61
NEAREST NEIGHBOR	0.21 / 0.29	0.26 / 0.37	0.28 / 0.42	0.33 / 0.51	0.38 / 0.62
LINEAR INTERP.	0.19 / 0.23	0.23 / 0.30	0.26 / 0.34	0.30 / 0.42	0.36 / 0.51
LSM (MAE)	**0.15 / 0.11**	**0.15 / 0.12**	**0.16 / 0.13**	**0.17 / 0.15**	**0.19 / 0.17**
GAINS OVER INTERP.	**+21% / 52%**	**+35% / 60%**	**+38% / 62%**	**+43% / 64%**	**+47% / 67%**

(b) **Exercise Detection.**

Pretrain	**Probe/FT**	**Acc.**	**mAP**
-	RAND. FOREST	73.0	76.8
-	LOGISTIC REG.	72.4	67.3
-	SUPERVISED	70.9	61.7
MSN	Linear Probe	67.6	60.0
DINO	Linear Probe	66.0	57.0
SIMCLR	Linear Probe	66.5	51.5
LSM (MAE)	Linear Probe	84.7	89.0
MSN	Fine-tune	76.7	74.6
DINO	Fine-tune	78.2	80.3
SIMCLR	Fine-tune	74.9	66.6
LSM (MAE)	Fine-tune	**90.3**	**97.0**
GAIN OVER SUPERVISED		**+27%**	**+57%**

(c) **Activity Recognition.**

Pretrain	**Probe/FT**	**Acc.**	**mAP**
-	RAND. FOREST	56.5	43.1
-	LOGISTIC REG.	60.4	39.3
-	SUPERVISED	53.2	33.4
MSN	Linear Probe	44.6	24.0
DINO	Linear Probe	50.3	26.0
SIMCLR	Linear Probe	45.3	20.8
LSM (MAE)	Linear Probe	49.4	24.6
MSN	Fine-tune	62.5	43.4
DINO	Fine-tune	66.2	46.3
SIMCLR	Fine-tune	67.3	46.0
LSM (MAE)	Fine-tune	**68.5**	**51.4**
GAIN OVER SUPERVISED		**+29%**	**+54%**

All neural methods, including the supervised method, utilize a ViT-Base (110M) backbone. Relevant methods are pretrained with 6.6 million hours of data. In the sensor imputation task, we randomly mask 67% of the sensor modalities. MICE (Van Buuren & Groothuis-Oudshoorn, 2011), Random Forest (Breiman, 2001), MSN (Assran et al., 2022), DINO (Caron et al., 2021), SimCLR (Chen et al., 2020), MAE (He et al., 2022).

that these tasks remain highly challenging. Imputing large portions of missing data, especially over extended time intervals, often leads to degraded accuracy, with performance deteriorating as the missing data window increases. Similarly, extrapolation further into the future (e.g., several hours ahead) introduces significant uncertainty, making it difficult to predict fine-grained physiological or behavioral patterns. These findings suggest that while scaling helps improve generative capabilities, substantial challenges remain, particularly in handling long-range dependencies and large data gaps.

Are wearable foundation models label efficient on discriminative tasks? Our experiments on probing, fine-tuning, and few-shot learning for activity indicate that wearable foundation models are highly label efficient. As shown in Table 3(b), 3(c), and Appendix Table 14, the performance of the fine-tuned LSM consistently outperforms supervised baselines. A confusion matrix of the best performing model is shown in Fig. 7 of the Appendix. As shown in Table 11 of Appendix C.2, even in the low-data regime (e.g., 5-shot, 10-shot), foundation models demonstrate strong generalization

capabilities, achieving significantly lower error rates compared to models trained from scratch or with limited supervision. As the number of labeled examples increases, the performance gap widens, with foundation models leveraging pretraining to more effectively transfer learned representations to downstream tasks. T-distributed Stochastic Neighbor Embeddings (t-SNE) plots show the impact of pretraining on more data and fine-tuning are shown in Appendix C.4 (Fig. 8).

Why did models saturate? Our experiments indicate promising opportunities in scaling wearable sensor models but also highlight several unresolved questions. Notably, we observe saturation in scaling laws with a dataset size of 10^7 hours and model sizes in 100 millions. We attribute this to three factors: (1) the current pretraining task may not be sufficiently scalable, and decoder-only approaches might better leverage data rather than filling masked inputs; (2) the dataset construction lacks sufficient challenge, and extending the sensor context window from 5 hours to a day or even a week could introduce more complexity that enables the model to learn longer time dependency relationships; (3) our data cleaning process was minimal, and increasing data diversity, akin to large-scale language model training, could significantly enhance model generalization. For example, while our dataset spanned all four seasons, there was an imbalance in temporal coverage, with two years of data from January to June but only a single year from July to December. This uneven distribution could bias the model towards activities more common in the earlier part of the year.

Additional discussions regarding scaling LSM to the edge can be found in Appendix D. Additional results of model design choice are presented in Appendix A. Qualitative examples of signal and embedding are provided in Appendix C.4 & C.6.

6 Limitations & Future Work

A key characteristic of wearable sensor data is its inherent missingness. Handling missing data in both pretraining and downstream tasks remains an open question. While we used imputation for this study, a more principled approach would involve designing models that naturally account for missing data without introducing imputation biases. The nature of missing data in wearable sensors often correlates with real-world events (e.g., charging the device, loose fitting), which can mean that data is missing not at random (MNAR). We recognize our study does not have a deep investigation on various of missingness in wearable data, understanding these factors and designing methods to handle them robustly remains an important direction for future work. Lastly, we acknowledge the lack of comprehensive evaluation on more discriminative tasks and diverse set of wearable devices. Future work will expand the dataset to include a broader range of classification and regression tasks across different dataset sources and devices.

We acknowledge that creating generic input representations for data from different sensors, each with unique properties, is challenging. This motivated our choice to build the model on minutely features derived from raw sensor data, which inherently vary in sampling rates. These features can be similarly derived from a wide range of sensors, making the inputs somewhat device-agnostic. However, wearable signals in their raw form (e.g., 120Hz accelerometer values) often exhibit strong periodicity, which is not retained in the aggregated minutely features. As a result, we focused on time-domain representations for our inputs, but we acknowledge that this approach may not fully leverage the fine-grained temporal or spectral characteristics of raw signals, potentially limiting generalization across diverse modalities and resolutions. We acknowledge that the 5-hour window represents a trade-off, balancing the complexity needed for pretraining with the temporal specificity required for downstream tasks. Future work will explore task-specific window sizes, refined masking strategies to better align with the temporal characteristics of downstream events, and the ability of these models to generalize across wearable devices with varying sensor capabilities.

7 Conclusion

We present LSM, a large multimodal foundation model trained on 40 million hours of wearable sensor data from over 165,000 individuals, establishing scaling laws for sensor models. LSM improves performance across generative tasks and discriminative tasks. Our results demonstrate that scaling data, model size, and compute leads to substantial gains in generalization and efficiency. LSM highlights the potential of scaling wearable sensor models for real-world health applications.

BIBLIOGRAPHY

Salar Abbaspourazad, Oussama Elachqar, Andrew Miller, Saba Emrani, Udhyakumar Nallasamy, and Ian Shapiro. Large-scale training of foundation models for wearable biosignals. In *The Twelfth International Conference on Learning Representations*, 2023.

Rebecca Adaimi, Abdelkareem Bedri, Jun Gong, Richard Kang, Joanna Arreaza-Taylor, Gerri-Michelle Pascual, Michael Ralph, and Gierad Laput. Advancing location-invariant and device-agnostic motion activity recognition on wearable devices. *arXiv preprint arXiv:2402.03714*, 2024.

Deepak Adhikari, Wei Jiang, Jinyu Zhan, Zhiyuan He, Danda B Rawat, Uwe Aickelin, and Hadi A Khorshidi. A comprehensive survey on imputation of missing data in internet of things. *ACM Computing Surveys*, 55(7):1–38, 2022.

Armen Aghajanyan, Lili Yu, Alexis Conneau, Wei-Ning Hsu, Karen Hambardzumyan, Susan Zhang, Stephen Roller, Naman Goyal, Omer Levy, and Luke Zettlemoyer. Scaling laws for generative mixed-modal language models. In *International Conference on Machine Learning*, pp. 265–279. PMLR, 2023.

Abdul Fatir Ansari, Lorenzo Stella, Caner Turkmen, Xiyuan Zhang, Pedro Mercado, Huibin Shen, Oleksandr Shchur, Syama Sundar Rangapuram, Sebastian Pineda Arango, Shubham Kapoor, et al. Chronos: Learning the language of time series. *arXiv preprint arXiv:2403.07815*, 2024.

Mahmoud Assran, Mathilde Caron, Ishan Misra, Piotr Bojanowski, Florian Bordes, Pascal Vincent, Armand Joulin, Mike Rabbat, and Nicolas Ballas. Masked siamese networks for label-efficient learning. In *European Conference on Computer Vision*, pp. 456–473. Springer, 2022.

Melissa J Azur, Elizabeth A Stuart, Constantine Frangakis, and Philip J Leaf. Multiple imputation by chained equations: what is it and how does it work? *International journal of methods in psychiatric research*, 20(1):40–49, 2011.

Yasaman Bahri, Ethan Dyer, Jared Kaplan, Jaehoon Lee, and Utkarsh Sharma. Explaining neural scaling laws. *Proceedings of the National Academy of Sciences*, 121(27):e2311878121, 2024.

Leo Breiman. Random forests. *Machine learning*, 45:5–32, 2001.

Tadeusz Caliński and Jerzy Harabasz. A dendrite method for cluster analysis. *Communications in Statistics-theory and Methods*, 3(1):1–27, 1974.

Mathilde Caron, Piotr Bojanowski, Armand Joulin, and Matthijs Douze. Deep clustering for unsupervised learning of visual features. In *Proceedings of the European conference on computer vision (ECCV)*, pp. 132–149, 2018.

Mathilde Caron, Hugo Touvron, Ishan Misra, Hervé Jégou, Julien Mairal, Piotr Bojanowski, and Armand Joulin. Emerging properties in self-supervised vision transformers. In *Proceedings of the IEEE/CVF international conference on computer vision*, pp. 9650–9660, 2021.

Melvin D Cheitlin. Cardiovascular physiology—changes with aging. *The American journal of geriatric cardiology*, 12(1):9–13, 2003.

Ting Chen, Simon Kornblith, Mohammad Norouzi, and Geoffrey Hinton. A simple framework for contrastive learning of visual representations. In *International conference on machine learning*, pp. 1597–1607. PMLR, 2020.

Abhimanyu Das, Weihao Kong, Rajat Sen, and Yichen Zhou. A decoder-only foundation model for time-series forecasting. *arXiv preprint arXiv:2310.10688*, 2023.

Mostafa Dehghani, Alexey Gritsenko, Anurag Arnab, Matthias Minderer, and Yi Tay. Scenic: A jax library for computer vision research and beyond. In *Proceedings of the IEEE/CVF Conference on Computer Vision and Pattern Recognition (CVPR)*, pp. 21393–21398, 2022.

Shohreh Deldari, Dimitris Spathis, Mohammad Malekzadeh, Fahim Kawsar, Flora D Salim, and Akhil Mathur. Crossl: Cross-modal self-supervised learning for time-series through latent masking. In *Proceedings of the 17th ACM International Conference on Web Search and Data Mining*, pp. 152–160, 2024.

Alexey Dosovitskiy. An image is worth 16x16 words: Transformers for image recognition at scale. *arXiv preprint arXiv:2010.11929*, 2020.

Paul Ekman, Robert W Levenson, and Wallace V Friesen. Autonomic nervous system activity distinguishes among emotions. *science*, 221(4616):1208–1210, 1983.

Azul Garza and Max Mergenthaler-Canseco. Timegpt-1. *arXiv preprint arXiv:2310.03589*, 2023.

Anda Gershon, Nilam Ram, Sheri L Johnson, Allison G Harvey, and Jamie M Zeitzer. Daily actigraphy profiles distinguish depressive and interepisode states in bipolar disorder. *Clinical psychological science*, 4(4):641–650, 2016.

Mononito Goswami, Konrad Szafer, Arjun Choudhry, Yifu Cai, Shuo Li, and Artur Dubrawski. Moment: A family of open time-series foundation models. *arXiv preprint arXiv:2402.03885*, 2024.

Dianyuan Han. Comparison of commonly used image interpolation methods. In *Conference of the 2nd International Conference on Computer Science and Electronics Engineering (ICCSEE 2013)*, pp. 1556–1559. Atlantis Press, 2013.

Harish Haresamudram, Irfan Essa, and Thomas Plötz. Contrastive predictive coding for human activity recognition. *Proceedings of the ACM on Interactive, Mobile, Wearable and Ubiquitous Technologies*, 5(2):1–26, 2021.

Kaiming He, Xinlei Chen, Saining Xie, Yanghao Li, Piotr Dollár, and Ross Girshick. Masked autoencoders are scalable vision learners. In *Proceedings of the IEEE/CVF conference on computer vision and pattern recognition*, pp. 16000–16009, 2022.

Tom Henighan, Jared Kaplan, Mor Katz, Mark Chen, Christopher Hesse, Jacob Jackson, Heewoo Jun, Tom B Brown, Prafulla Dhariwal, Scott Gray, et al. Scaling laws for autoregressive generative modeling. *arXiv preprint arXiv:2010.14701*, 2020.

Joel Hestness, Sharan Narang, Newsha Ardalani, Gregory Diamos, Heewoo Jun, Hassan Kianinejad, Md Mostofa Ali Patwary, Yang Yang, and Yanqi Zhou. Deep learning scaling is predictable, empirically. *arXiv preprint arXiv:1712.00409*, 2017.

Po-Yao Huang, Hu Xu, Juncheng Li, Alexei Baevski, Michael Auli, Wojciech Galuba, Florian Metze, and Christoph Feichtenhofer. Masked autoencoders that listen. *Advances in Neural Information Processing Systems*, 35:28708–28720, 2022.

Lawrence Hubert and Phipps Arabie. Comparing partitions. *Journal of classification*, 2:193–218, 1985.

Jared Kaplan, Sam McCandlish, Tom Henighan, Tom B Brown, Benjamin Chess, Rewon Child, Scott Gray, Alec Radford, Jeffrey Wu, and Dario Amodei. Scaling laws for neural language models. *arXiv preprint arXiv:2001.08361*, 2020.

Wei Yang Bryan Lim, Nguyen Cong Luong, Dinh Thai Hoang, Yutao Jiao, Ying-Chang Liang, Qiang Yang, Dusit Niyato, and Chunyan Miao. Federated learning in mobile edge networks: A comprehensive survey. *IEEE communications surveys & tutorials*, 22(3):2031–2063, 2020.

Xin Liu, Daniel McDuff, Geza Kovacs, Isaac Galatzer-Levy, Jacob Sunshine, Jiening Zhan, Ming-Zher Poh, Shun Liao, Paolo Di Achille, and Shwetak Patel. Large language models are few-shot health learners. *arXiv preprint arXiv:2305.15525*, 2023.

I Loshchilov. Decoupled weight decay regularization. *arXiv preprint arXiv:1711.05101*, 2017.

Steven A Lubitz, Anthony Z Faranesh, Caitlin Selvaggi, Steven J Atlas, David D McManus, Daniel E Singer, Sherry Pagoto, Michael V McConnell, Alexandros Pantelopoulos, and Andrea S Foulkes. Detection of atrial fibrillation in a large population using wearable devices: the fitbit heart study. *Circulation*, 146(19):1415–1424, 2022.

Daniel McDuff, Seamus Thomson, Samy Abdel-Ghaffar, Isaac Galatzer-Levy, Ming-Zher Poh, Jake Sunshine, Andrew Barakat, Conor Heneghan, and Lindsey Sunden. What does large-scale electrodermal sensing reveal? *bioRxiv*, pp. 2024–02, 2024.

Mika A Merrill and Tim Althoff. Self-supervised pretraining and transfer learning enable\titlebreak flu and covid-19 predictions in small mobile sensing datasets. In *Conference on Health, Inference, and Learning*, pp. 191–206. PMLR, 2023.

Mike A Merrill, Mingtian Tan, Vinayak Gupta, Tom Hartvigsen, and Tim Althoff. Language models still struggle to zero-shot reason about time series. *arXiv preprint arXiv:2404.11757*, 2024.

Bernard Munos, Pamela C Baker, Brian M Bot, Michelle Crouthamel, Glen de Vries, Ian Ferguson, John D Hixson, Linda A Malek, John J Mastrototaro, Veena Misra, et al. Mobile health: the power of wearables, sensors, and apps to transform clinical trials. *Annals of the New York Academy of Sciences*, 1375(1):3–18, 2016.

Girish Narayanswamy, Yujia Liu, Yuzhe Yang, Chengqian Ma, Xin Liu, Daniel McDuff, and Shwetak Patel. Bigsmall: Efficient multi-task learning for disparate spatial and temporal physiological measurements. In *Proceedings of the IEEE/CVF Winter Conference on Applications of Computer Vision*, pp. 7914–7924, 2024.

Aravind Natarajan, Alexandros Pantelopoulos, Hulya Emir-Farinas, and Pradeep Natarajan. Heart rate variability with photoplethysmography in 8 million individuals: a cross-sectional study. *The Lancet Digital Health*, 2(12):e650–e657, 2020.

Michael Nissen, Syrine Slim, Katharina Jäger, Madeleine Flaucher, Hanna Huebner, Nina Danzberger, Peter A Fasching, Matthias W Beckmann, Stefan Gradl, Bjoern M Eskofier, et al. Heart rate measurement accuracy of fitbit charge 4 and samsung galaxy watch active2: device evaluation study. *JMIR formative research*, 6(3):e33635, 2022.

Mehdi Noroozi, Hamed Pirsiavash, and Paolo Favaro. Representation learning by learning to count. In *Proceedings of the IEEE international conference on computer vision*, pp. 5898–5906, 2017.

Colin Raffel, Noam Shazeer, Adam Roberts, Katherine Lee, Sharan Narang, Michael Matena, Yanqi Zhou, Wei Li, and Peter J Liu. Exploring the limits of transfer learning with a unified text-to-text transformer. *Journal of machine learning research*, 21(140):1–67, 2020.

Aniruddh Raghu, Payal Chandak, Ridwan Alam, John Guttag, and Collin Stultz. Sequential multi-dimensional self-supervised learning for clinical time series. In *International Conference on Machine Learning*, pp. 28531–28548. PMLR, 2023.

Kashif Rasul, Arjun Ashok, Andrew Robert Williams, Arian Khorasani, George Adamopoulos, Rishika Bhagwatkar, Marin Biloš, Hena Ghonia, Nadhir Vincent Hassen, Anderson Schneider, et al. Lag-llama: Towards foundation models for time series forecasting. *arXiv preprint arXiv:2310.08278*, 2023.

Jiawei Ren, Cunjun Yu, Shunan Sheng, Xiao Ma, Haiyu Zhao, Shuai Yi, and Hongsheng Li. Balanced meta-softmax for long-tailed visual recognition. In *Proceedings of Neural Information Processing Systems(NeurIPS)*, Dec 2020.

Mickael Ringeval, Gerit Wagner, James Denford, Guy Paré, and Spyros Kitsiou. Fitbit-based interventions for healthy lifestyle outcomes: systematic review and meta-analysis. *Journal of medical Internet research*, 22(10):e23954, 2020.

Aaqib Saeed, Victor Ungureanu, and Beat Gfeller. Sense and learn: Self-supervision for omnipresent sensors. *Machine Learning with Applications*, 6:100152, 2021.

Fred Shaffer and Jay P Ginsberg. An overview of heart rate variability metrics and norms. *Frontiers in public health*, 5:258, 2017.

Dimitris Spathis, Ignacio Perez-Pozuelo, Soren Brage, Nicholas J Wareham, and Cecilia Mascolo. Self-supervised transfer learning of physiological representations from free-living wearable data. In *Proceedings of the Conference on Health, Inference, and Learning*, pp. 69–78, 2021.

Rahul Thapa, Bryan He, Magnus Ruud Kjaer, Hyatt Moore, Gauri Ganjoo, Emmanuel Mignot, and James Zou. Sleepfm: Multi-modal representation learning for sleep across brain activity, ecg and respiratory signals. *arXiv preprint arXiv:2405.17766*, 2024.

Stef Van Buuren and Karin Groothuis-Oudshoorn. mice: Multivariate imputation by chained equations in r. *Journal of statistical software*, 45:1–67, 2011.

Mathilde C van Rossum, Pedro M Alves da Silva, Ying Wang, Ewout A Kouwenhoven, and Hermie J Hermens. Missing data imputation techniques for wireless continuous vital signs monitoring. *Journal of clinical monitoring and computing*, 37(5):1387–1400, 2023.

Nguyen Xuan Vinh, Julien Epps, and James Bailey. Information theoretic measures for clusterings comparison: is a correction for chance necessary? In *Proceedings of the 26th annual international conference on machine learning*, pp. 1073–1080, 2009.

Zhenda Xie, Zheng Zhang, Yue Cao, Yutong Lin, Yixuan Wei, Qi Dai, and Han Hu. On data scaling in masked image modeling. In *Proceedings of the IEEE/CVF Conference on Computer Vision and Pattern Recognition*, pp. 10365–10374, 2023.

Jiajun Xu, Zhiyuan Li, Wei Chen, Qun Wang, Xin Gao, Qi Cai, and Ziyuan Ling. On-device language models: A comprehensive review. *arXiv preprint arXiv:2409.00088*, 2024.

Yuzhe Yang, Yuan Yuan, Guo Zhang, Hao Wang, Ying-Cong Chen, Yingcheng Liu, Christopher G Tarolli, Daniel Crepeau, Jan Bukartyk, Mithri R Junna, et al. Artificial intelligence-enabled detection and assessment of parkinson's disease using nocturnal breathing signals. *Nature Medicine*, 28(10):2207–2215, 2022.

Yuzhe Yang, Xin Liu, Jiang Wu, Silviu Borac, Dina Katabi, Ming-Zher Poh, and Daniel McDuff. Simper: Simple self-supervised learning of periodic targets. In *The Eleventh International Conference on Learning Representations*, 2023.

Hang Yuan, Shing Chan, Andrew P Creagh, Catherine Tong, Aidan Acquah, David A Clifton, and Aiden Doherty. Self-supervised learning for human activity recognition using 700,000 person-days of wearable data. *NPJ digital medicine*, 7(1):91, 2024.

Xiaohua Zhai, Alexander Kolesnikov, Neil Houlsby, and Lucas Beyer. Scaling vision transformers. In *Proceedings of the IEEE/CVF conference on computer vision and pattern recognition*, pp. 12104–12113, 2022.

APPENDIX

A MODEL DESIGN CHOICES AND ABLATIONS

We perform ablations on the configurations used for our masked autoencoder LSM design. Following the convention of previous works (He et al., 2022; Huang et al., 2022), we explore masking ratio, masking strategies, patch sizes, and model sizes. Uniquely, we explore the ordering of sensor signals, as these signals do not share the same explicit ordered dependencies as exist in images and audio spectrograms. For all experiments we employ random masking, a 0.8 masking ratio, ordered sensor signal order, a patch size of 10x5, and a LSM-Base (110M) backbone, unless otherwise specified.

A.1 SELECTING A MASKING RATIO

Selecting the appropriate masking ratio is critical for ensuring effective representation learning in our sensor MAE training. We explore different masking ratios, ranging from 30% to 90%, to evaluate their impact on reconstruction quality and model generalization. We find that a masking ratio of 80% yields the best performance on temporal interpolation and extrapolation as shown in Table 4).

Table 4: **Ablation study of masking ratios.**

Mask Ratio	Interpolation 60 mins		Extrapolation 60 mins	
	MAE	MSE	MAE	MSE
0.3	0.29	0.31	0.38	0.47
0.4	0.35	0.39	0.38	0.45
0.5	0.25	0.27	0.39	0.46
0.6	0.44	0.57	0.38	0.45
0.7	0.40	0.51	**0.37**	**0.44**
0.8	**0.24**	**0.26**	**0.37**	**0.44**
0.9	0.31	0.33	0.40	0.49

A.2 SELECTING A MASKING STRATEGY

To train a wearable foundation model effective for both generative and discriminative tasks, mask-based pretraining proves superior to contrastive pretraining. Choosing the right masking strategy is crucial, as it directly influences the quality of the learned embeddings and the model's generalizability. In Table 5, we systematically compare five different masking strategies and demonstrate that random masking consistently yields the best performance across the two primary generative tasks. Example visualizations of these masking strategies can be seen in Fig. 5.

Table 5: **Ablation study of masking strategies.**

Mask Strategy	Interpolation 60 mins		Extrapolation 60 mins	
	MAE	MSE	MAE	MSE
RANDOM	**0.24**	**0.26**	**0.37**	**0.44**
STRUCTURED (TEMPORAL)	**0.24**	**0.26**	**0.37**	**0.44**
STRUCTURED (SENSOR)	0.54	0.71	0.53	0.73
TEMPORAL INTERPOLATION	0.41	0.48	0.52	0.66
TEMPORAL EXTRAPOLATION	0.43	0.51	0.51	0.64

A.3 SELECTING A SENSOR SIGNAL ORDER

For multimodal sensor data, the order in which signals are processed by the model can impact performance. Specifically, for architectures, such as vision transformers, that take patched inputs,

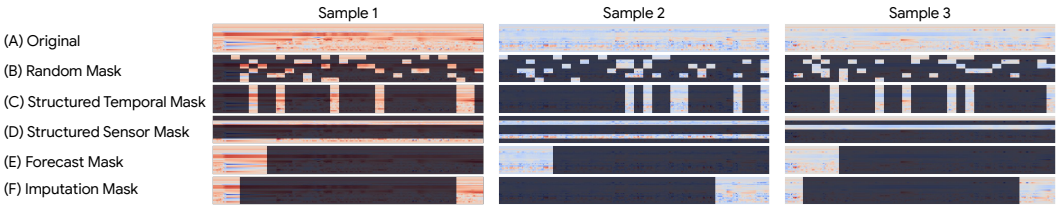

Figure 5: LSM **MAE pretrain masking strategies.** All strategies employ a masking ratio of 0.8. **(A)**: original, unmasked sensor image, **(B)**: random masking, **(C)**: structured temporal masking, **(D)**: structured sensor masking, **(E)**: temporal extrapolation masking, **(F)**: temporal interpolation masking. Both random and structured temporal masking enable strong down-stream performance. We select random masking for all scaling experiments and evaluations.

the clustering of signals in patches may have a profound impact on the learned representation. We evaluate ordering the sensor signals by: (a) sensor types (as in Table 18), (b) randomized order (repeated with several random seeds) and (c) interleaving signals with uncorrelated signals. Cross correlation matrices are shown in Fig. 10. We find that ordering by clustering sensor type generally yields better results (see Table 6), particularly when dealing with heterogeneous sensor modalities like accelerometry, electrodermal activity (EDA), and heart rate. This order allows the model to leverage specific sensor characteristics more effectively, improving performance on downstream tasks.

Table 6: **Ablation study of sensor orders.**

Sensor Order	Interpolation 60 mins		Extrapolation 60 mins	
	MAE	MSE	MAE	MSE
CLUSTERED	**0.24**	**0.26**	**0.37**	**0.44**
RANDOMIZED (N=5)	0.28	0.32	0.38	0.45
MAX ENTROPY	0.30	0.34	0.45	0.55

A.4 SELECTING A PATCH SIZE.

Patch size in our pretraining is defined by time steps and the number of sensor features per patch, both impacting model capacity and computation (gFlops). In contrast to previous works (He et al., 2022; Huang et al., 2022) we expensively sweep across both dimensions of the input. This is critical for sensor models, where both dimensions, of time and features, share unique correlations and dependencies along their corresponding axis.

A time-step of 10 minutes strikes the best balance with low gFlops (15.94) and strong performance (MAE of 0.24 for imputation, 0.37 for forecasting) (See Table 7). Similarly, increasing features per patch shows that five features per patch achieves the best trade-off between accuracy and computational cost, outperforming both smaller (10x1) and larger patches (10x26). Thus, a moderate patch size of 10 minutes by 5 features is what we select.

As a patch-size of 10-minutes x 5-sensors (10x5) cannot evenly patch a input sensor-image of 300-minutes x 26-sensors (300x26), we zero-pad the sensor dimension to 30 resulting in an 300-minute x 30-feature (300x30) input sensor-image.

A.5 MODEL SIZE VARIANTS

In Table 8, we present four variants of the LSM models we trained. The model sizes and naming conventions partially follow the tradition established by T5 (Raffel et al., 2020). Our results indicate that scaling the model beyond LSM-B offers no additional improvements in either reconstruction loss or downstream task performance. Based on this insight all neural methods in Table 3 employ a ViT-110M backbone.

Table 7: **Ablation study of patch sizes.**

(a) **Sweep across time-steps per patch.** (5 feats. per patch)

Patch Size	gFlops	Interpolation 60 mins		Extrapolation 60 mins	
		MAE	MSE	MAE	MSE
5x5	33.09	0.34	0.41	**0.37**	0.46
10x5	15.94	**0.24**	**0.26**	**0.37**	**0.44**
20x5	7.82	0.26	0.28	0.41	0.48
30x5	**5.18**	0.28	0.30	**0.37**	**0.44**

(b) **Sweep across features per patch.** (10 mins. per patch)

Patch Size	gFlops	Interpolation 60 mins		Extrapolation 60 mins	
		MAE	MSE	MAE	MSE
10x1	77.83	0.30	0.33	0.43	0.53
10x2	36.07	0.30	0.33	0.45	0.53
10x5	15.94	**0.24**	**0.26**	**0.37**	**0.44**
10x10	7.82	0.33	0.38	0.45	0.55
10x26	**2.58**	0.28	0.31	0.43	0.51

Table 8: **Vision transformer size variants used in** `LSM`**.** An `LSM`-[size] model indicates a ViT-[size] backbone.

Model	Encoder Blocks	Decoder Blocks	Encoder Dim	Decoder Dim	Encoder Heads	Decoder Heads	Total Params	gFLOPs
`LSM`-Tiny	4	2	192	128	3	4	2M	0.37
`LSM`-Small	8	2	256	192	4	4	7M	1.28
`LSM`-Base	12	8	768	512	12	16	110M	15.94
`LSM`-Large	24	8	1,024	512	16	16	328M	56.10

B Additional Related Work

Learning from Multimodal Sensor Data. A significant body of work has explored representation learning for multimodal physiological time-series data from wearable devices. Spathis et al. (2021) employed pretext tasks to pre-train models on multimodal inputs such as heart rate and raw IMU signals, demonstrating their effectiveness across various downstream tasks. Saeed et al. (2021) introduced a self-supervised framework specifically designed for wearable sensors, emphasizing robustness through representation learning from diverse signal types. Deldari et al. (2024) proposed CrossL, a cross-modal self-supervised learning approach that utilizes latent masking to effectively model interactions between modalities. Haresamudram et al. (2021) applied contrastive predictive coding to human activity recognition, showcasing its capability to capture temporal dependencies in wearable sensor data. Further advancements include multitask learning for multi-dimensional clinical time series (Raghu et al., 2023) and physiological measurements (Narayanswamy et al., 2024). In contrast to prior work, our work emphasizes *scalable* modeling across a broader range of wearable sensor modalities and a significantly larger data sample size. We systematically investigate scaling behavior across compute, data size, and model capacity, and examine the generalizability of the learned representations on large-scale real-world datasets.

C Additional Results and Analysis

C.1 Results of Scaling Experiments for Generative Tasks

Generative Performance wrt. Data Scaling. Table 9 presents the full results for the generative tasks, evaluated across four model sizes and all data scales, including an experiment on the largest 40 million hour pretraining set. The `LSM` Base model, trained on 6.6 million hours of data, achieved the best overall performance.

Scaling Pretraining Data to 40 Million Hours. As mentioned in Sections 3 and 5, we derive our dataset, used for presented scaling and downstream task results from 6.6M hours of data balanced across 160K people. To test the extremes of data scaling we also build a dataset comprising of 40M data hours by combining the 6.6M hours with an additional 33M hours of data from a 78569 subject subset of the total 160K subjects. However, as shown in Table 9, we observed that scaling benefits taper off when training the `LSM`-Base model with this extended dataset. We believe this is due to two key factors: the structure of our dataset and the inherent limitations of the masking pretraining

task, as discussed in Section 6. It is also possible that as the additional 33M hours are not evenly distributed across subjects that the careful balance of the 6.6M dataset is disturbed.

C.2 Results of Scaling Experiments for Discriminative Tasks

Discriminative Performance wrt. Data Scaling. In Table 10, we demonstrate that scaling up the dataset significantly benefits downstream discriminative tasks, particularly in the fine-tuning stage. Furthermore, our pretrained LSM model exhibits superior performance in label-efficient transfer learning, as shown in Table 11. Activity recognition few-shot results, as compared to a supervised baseline, are also visualized in Fig. 6. From the visualization it is clear that pretraining helps LSM learn a strong representation of sensor data that enables more sample efficient performance on discriminative tasks.

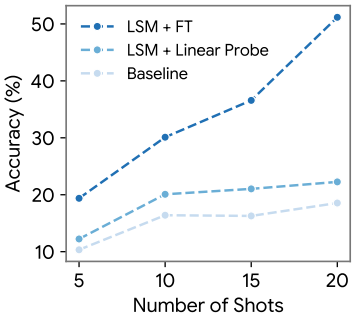

Figure 6: **Few shot learning.** Activity recognition results.

Convolutional Probe. Following prior work (He et al., 2022) we explore an intermediary evaluation to linear probing and full-model fine-tuning. Specifically, we explore the learnable pooling of embeddings. This probe takes patch-embeddings, produced by the encoder, and reshapes them to [num. patches H, num. patches W, embedding dimension], similar to the shape of the original patched sensor-image. This embedding is fed through two shallow convolutional layers and a linear head. We find that with less that 0.2% of the trainable-parameters needed for full-model fine-tuning, we are able to achieve similar performance on exercise detection and activity recognition tasks. These results can be seen in Tables 10 and 11.

Table 9: **Detailed Results of Generative Tasks.** Performance across Data and Model Sizes on Generative Tasks. Data Size is in hours.

Data Size	Model Size	Task Error (MSE)		
		Random Imputation 80%	Extrapolation 60 min	Interpolation 60 min
0.005 M	Tiny	0.50	0.71	0.53
	Small	0.57	0.77	0.62
	Base	0.67	0.80	0.68
	Large	0.64	0.82	0.75
0.05 M	Tiny	0.25	0.70	0.47
	Small	0.29	0.58	0.36
	Base	0.38	0.65	0.42
	Large	0.38	0.65	0.43
0.5 M	Tiny	0.22	0.62	0.42
	Small	0.21	0.53	0.37
	Base	0.22	0.48	0.28
	Large	0.22	0.50	0.34
3.8 M	Tiny	0.22	0.62	0.42
	Small	0.21	0.49	0.36
	Base	0.19	0.44	0.26
	Large	0.21	0.64	0.46
6.6 M	Tiny	0.22	0.63	0.42
	Small	0.21	0.49	0.35
	Base	0.19	0.44	0.26
	Large	0.20	0.54	0.40
40 M	Base	0.19	0.45	0.27

Table 10: **Data Scaling on Discriminative Tasks.**

Data Size	Method	Exercise Detection		Activity Recognition	
		Accuracy	mAP	Accuracy	mAP
0.005 M	Linear Probe	60.6	49.8	35.1	17.5
0.05 M		67.3	61.0	39.6	23.4
0.5 M		84.5	78.8	47.1	24.7
3.8 M		88.0	85.0	47.6	25.3
6.6 M		84.7	89.0	49.4	24.6
0.005 M	Convolutional Probe	71.3	71.8	50.9	25.1
0.05 M		78.0	82.3	62.2	43.7
0.5 M		88.2	96.4	68.1	45.5
3.8 M		88.2	96.4	70.5	47.1
6.6 M		87.5	95.8	67.6	48.5
0.005 M	Fine Tune	68.3	58.9	51.5	30.0
0.05 M		73.8	77.0	64.0	48.0
0.5 M		84.9	93.7	68.8	50.0
3.8 M		87.5	96.4	64.2	48.7
6.6 M		90.3	97.0	68.5	51.4

Table 11: **Few-Shot Performance on Discriminative Tasks.**

Samples per Class	Method	Exercise Detection		Activity Recognition	
		Accuracy	mAP	Accuracy	mAP
5	Linear Probe	51.3	48.0	12.2	17.5
10		58.3	57.1	20.1	18.4
15		65.4	68.8	21.0	18.7
20		65.1	69.8	22.3	18.8
5	Convolutional Probe	40.5	43.8	20.6	24.7
10		63.2	59.4	27.9	26.7
15		57.3	60.8	27.9	26.7
20		67.0	56.9	36.9	25.3
5	Fine Tune	54.7	56.8	19.4	21.5
10		65.8	65.1	30.1	22.7
15		71.1	73.1	36.6	24.8
20		65.6	67.1	51.2	33.2
5	Supervised	43.1	52.9	10.3	14.5
10		49.3	46.0	16.4	14.6
15		49.6	50.6	16.3	14.4
20		48.2	45.8	18.5	23.0

C.3 Classification Confusion Matrices

Fig. 7 presents the complete confusion matrix for our activity recognition task from the full-model fine-tuned `LSM`-B model. Note that many classes get mistaken for *Walk*. This is likely as there are significant periods of walking in the 5-hour inputs, even if the activity is labeled otherwise.

C.4 Feature Embeddings

We present t-distributed Stochastic Neighbor Embedding (t-SNE) plots. In Fig. 8 illustrates that scaling pretraining data results in noticeable, albeit subtle, improvements of clustering across activ-

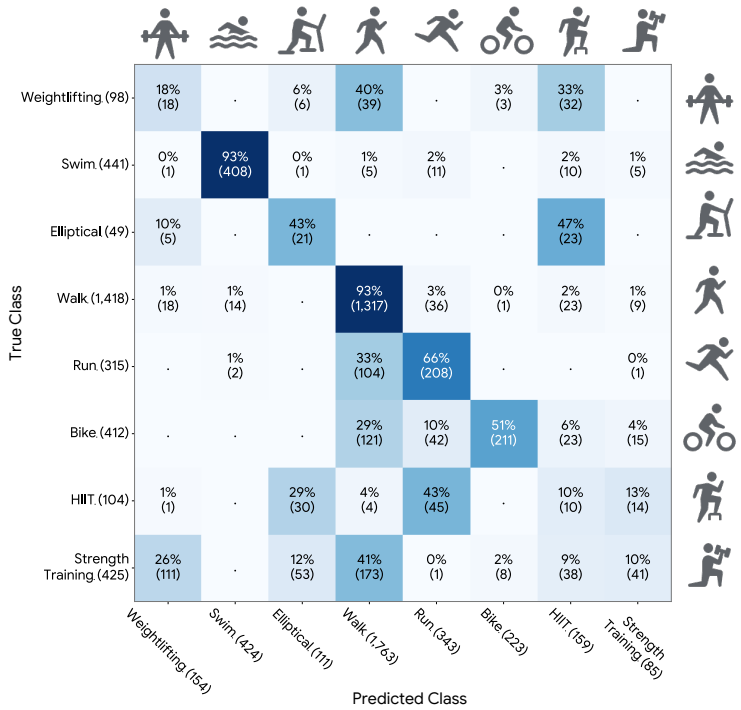

Figure 7: **Activity recognition confusion matrix.** Results for the full-model fined-tuned `LSM` Masked Auto-Encoder.

ities in the learned representation. We also find that fine-tuning the model is critical to effectively discriminate between activities. In Fig. 9 we see that the learned representation does embed some subject dependencies. This can be attributed to variance in the physiology and activity definitions for individuals (e.g., a hard run may look very different for two different people). We present quantitative results of a subset of these embeddings in Table 12.

Table 12: **Measures of Embedding Clustering**. These quantitative evaluations of embedding clustering support the claim that there are subtle differences in embeddings pretrained on different scales of data, as visualize in Fig. 8.

Finetune	Pretrain Size (Hrs)	Pretrain Size (People)	Calinski-Harabasz ↑	ARI ↑	NMI ↑
No	49K	1K	11508	0.026	0.083
No	6.6M	132K	11855	0.034	0.113
Yes	49K	1K	11972	0.256	0.465
Yes	6.6M	132K	11993	0.253	0.501

Calinski-Harabasz Score (Caliński & Harabasz, 1974), Adjusted Rand Index (ARI) (Hubert & Arabie, 1985), Normalized Mutual Information Score (NMI) (Vinh et al., 2009).

C.5 Signal Correlations

The 26 signals used as input to our model come from four sensors (accelerometer, PPG, temperature, altimeter). As a result, some signals are more correlated with certain ones than with others.. A signal diagonal correlation matrix was calculated to show the pairwise correlations between signals. Fig. 10 shows the correlation matrix for signals clustered by sensor and for signals ordered to minimize the absolute correlation coefficient between adjacent features.

C.6 Examples of Reconstructions

A qualitative example of ground-truth signals and corresponding reconstructions are shown in Fig. 11. The gray regions are sections that were masked in the input. Additional sensor-image level

Figure 8: **t-SNE Embeddings for Pretraining and Fine-tuned Models Labeled by Activity.** t-distributed Stochastic Neighbor Embedding (t-SNE) plots showing that there are differences (albeit subtle) between pretrained embeddings using data from almost 50k and 6.6 hours.

reconstructions, across generative down-stream tasks (eg. imputation, extrapolation, interpolation) can be seen in Fig. 12. Examples of the often visually subtle affects of scaling on reconstruction can be seen in Fig. 13.

C.7 Additional Discriminative Tasks

Here we discuss the additional discriminative tasks of sex and age classification, and subject dependent mood recognition. The datasets for these tasks are presented in Table 13. The performance of our methods and baselines are presented in Table 14.

Biological Sex Classification. Biological sex classification attempts to categorize an individuals as either *Female*, or *Male* from a sample of their wearable data. Though we do not explicitly intend our learnt representation to encode this information this discriminative tasks may allude to a methods ability to understand some-sense of differences in human biology. This experiment mirrors those conducted by similar works (Abbaspourazad et al., 2023).

Figure 9: **t-SNE Embeddings Labeled by Gender, Age and Subject.** t-distributed Stochastic Neighbor Embedding (t-SNE) plots showing that the learned embeddings do capture subject specific information (and therefore also exhibit some subtle gender and age clusters). Age was not available for all subjects.

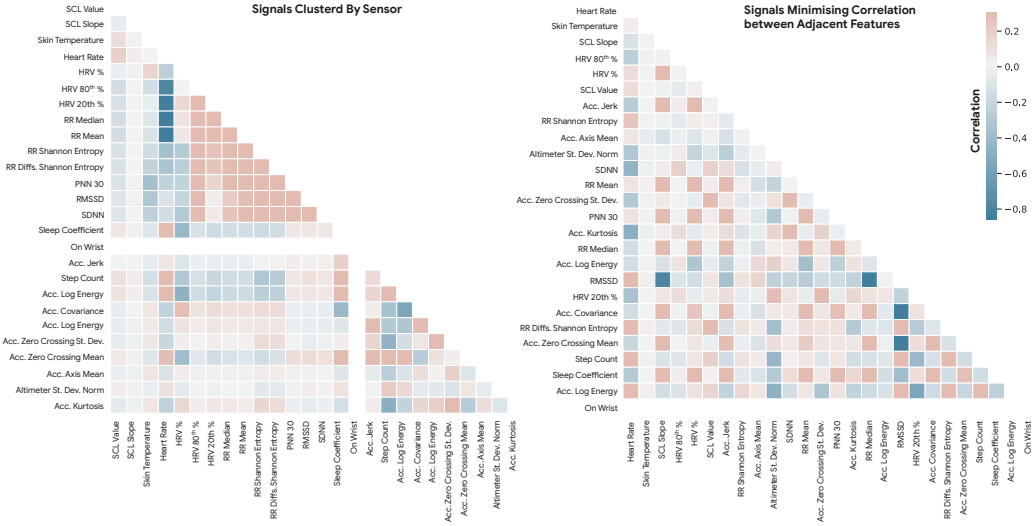

Figure 10: **Sensor Signal Diagonal Correlation Matrix.** The pair-wise correlation between the 26 sensor features based on our training set.

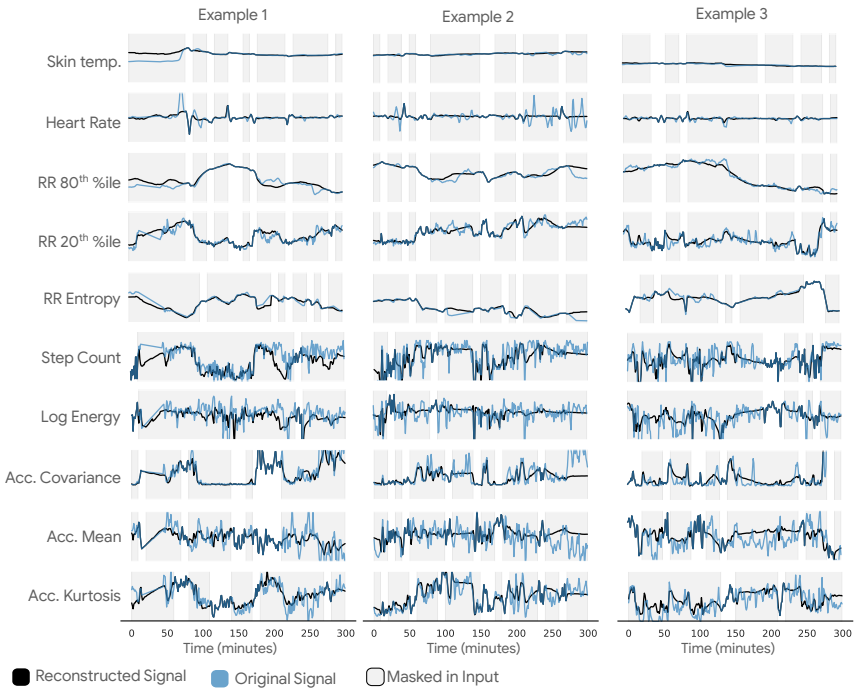

Figure 11: **Example of Signal Reconstructions.** Comparison between the ground-truth (blue) and reconstruction (black) for a 5-hour sample. Gray regions were masked in the input. 80% Random Masking (Patch Size 10 mins x 5 sensors). Note: model outputs are only shown for the masked regions in the reconstructions.

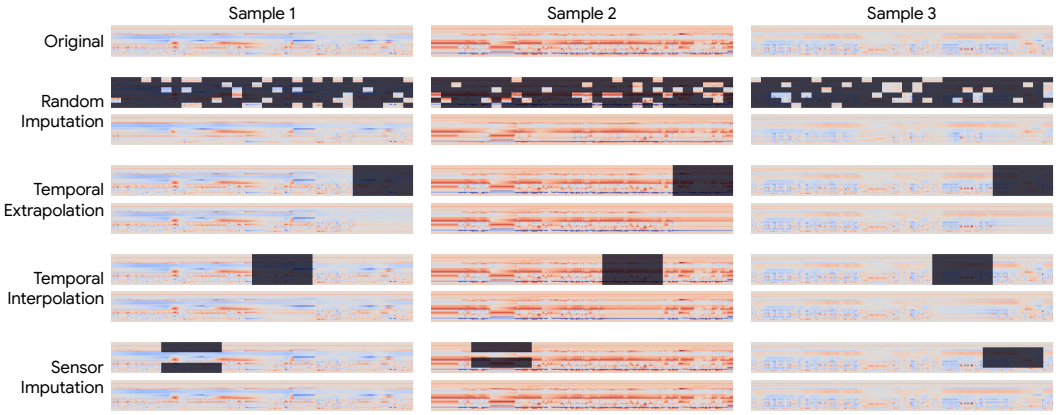

Figure 12: **Examples of Signal Reconstructions Across Generative Down Stream Tasks.** The top row of each sample shows the original sensor signal image. Subsequent row-pairs plot the masked input followed by the model reconstruction below. All reconstruction come from LSM-Base based LSM employing a 10x5 patch size and pretrained with 80% random masking. Note: model outputs are only shown for the masked patches in the reconstructions.

Binned Age Classification. Binned age classification defines 4 discrete age buckets. These binned ranges are [18 - 34], [35 - 49], [50 - 64], 65+. Although our pre-training methods do not explicitly intend to learn age, there are known correlations between a persons age and their physiological state (Cheitlin, 2003). To this end, the task of binned age classification provides a proxy signal to understand the extent to which a system is able to model differences in physiology. This experiment mirrors those conducted by similar works (Abbaspourazad et al., 2023).

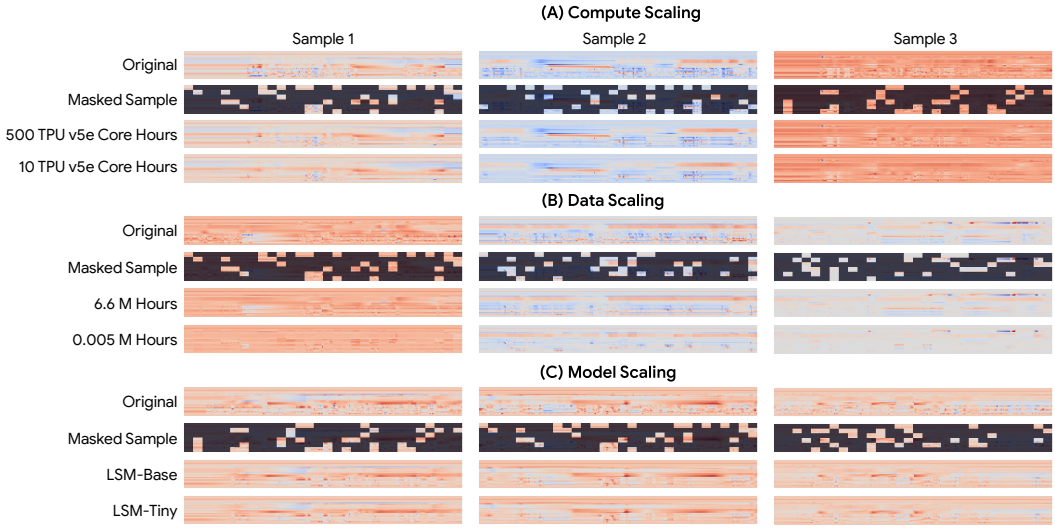

Figure 13: **Examples of Signal Reconstructions with Respect to Scaling.** These plots illustrate the (often visually subtle) affect of **A** compute, **B** data, and **C** model scaling for sensor models. Note: model outputs are only shown for the masked patches in the reconstructions.

Subject Dependent Mood Recognition. Mood recognition is the processes of categorizing a person's emotion events given patterns detected in their sensor data. Such mood events may causes changes in the activity of the autonomic nervous system and thus result in measurable physiological changes (Ekman et al., 1983). Our dataset includes five user-labeled mood states: *Content, Frustrated, Excited, Calm, Stressed*. We find, however, that these mood events vary significantly from person to person. This is likely due to the innate ambiguity associated with people's emotions. For example, one person's *Frustration* may easily be construed as *Stress* by another. Motivated by this, we focus on the task of subject dependent mood recognition, where for a given person their mood event samples are split 80-20 between train-test sets.

Table 13: **Details of additional discriminative datasets.** Summary of class distributions for our additional discriminative task datasets.

Task	Class	# Training	# Testing
Sex	Female	9,181	2,160
	Male	5,022	1,090
	Total	14,203	3,250
Age	18-35	1,179	499
	35-49	5,697	793
	50-64	5,246	1,297
	$\geq$ 65	2,250	673
Mood	Content	786	238
	Frustrated	460	199
	Excited	408	118
	Calm	767	265
	Stressed	1,132	334
	Total	3,553	1,154
	Total	14,372	3,262

D Additional Discussions, and Future Work

Table 14: **Comparisons of LSM and competing methods on the discriminative tasks of biological sex classification, binned age classification, and subject dependent mood recognition.**

Pretrain	Probe/FT	Sex Classification		Age Classification		Mood Recognition	
		Acc.	mAP	Acc.	mAP	Acc.	mAP
-	RANDOM FOREST	66.2	56.6	**42.3**	35.3	41.8	**44.4**
-	LOGISTIC REGRESSION	59.9	54.0	28.9	28.5	43.5	42.8
-	SUPERVISED	66.0	60.1	35.3	33.4	42.4	32.7
MSN	Linear Probe	68.0	61.9	36.4	29.2	36.7	34.8
DINO	Linear Probe	66.4	64.6	31.0	29.9	40.6	36.5
SIMCLR	Linear Probe	67.6	60.3	37.6	26.3	36.2	30.1
LSM (MAE)	Linear Probe	**75.4**	75.3	40.9	38.2	42.0	34.7
MSN	Fine-tune	68.3	63.8	43.8	36.6	41.2	38.8
DINO	Fine-tune	67.9	60.9	36.9	34.4	43.5	37.9
SIMCLR	Fine-tune	65.2	57.6	37.3	33.5	43.8	37.4
LSM (MAE)	Fine-tune	**75.4**	**79.8**	42.2	**38.7**	**49.0**	43.0
GAIN OVER SUPERVISED		**+14.1%**	**+32.8%**	**+19.5%**	**+15.9%**	**+15.6%**	**+31.5%**

All neural methods, including the supervised method, utilize a ViT-Base (110M) backbone. Relevant methods are pretrained with 6.6 million hours of data. In the sensor imputation task, we randomly mask 67% of the sensor modalities. Random Forest (Breiman, 2001), ViT (Dosovitskiy, 2020), MSN (Assran et al., 2022), DINO (Caron et al., 2021), SimCLR (Chen et al., 2020), MAE (He et al., 2022).

D.1 DISCUSSIONS

Can Wearable Foundation Models Scale to Edge Devices? Our model saturation in 110M parameters highlights a practical advantage: models of this size can potentially run in real-time on modern mobile devices, leveraging advancements in on-device large language models that often exceed 1 billion parameters in on-device deployments (Xu et al., 2024). We further note that the strong performance of statistical machine learning baselines, on classification tasks, indicate that there may be utility in distilling LSM to be smaller and more edge-performant. Additionally, unlike prior research focused on raw sensor data (e.g., (Yuan et al., 2024)), our results establish that scaling is effective with per-minute aggregated data. This approach not only reduces privacy risks but also introduces a standardized format that is easier to unify across platforms and devices. Looking forward, these findings open the door to collaborative efforts such as federated learning (Lim et al., 2020) across different wearable manufacturers, enabling scalable, privacy-preserving training while maintaining compatibility across diverse hardware ecosystems.

D.2 FUTURE WORK

The Effect of Missing Data on Discriminative Tasks. As previously mentioned, missingness is inherent in wearable sensor data. This may occur due sporadic, un-planned events such as battery depletion, environmental factors (e.g. extreme temperatures), or due to planned events such as charging one's device at night. To this end our current evaluation utilizes missingness during MAE pretraining. However, we do not explore the ability of missing data to affect downstream classification tasks. Future work may explore the tolerance of LSM like models to missingness and the ability of these models to provide accurate classifications based on incomplete data.

E ADDITIONAL IMPLEMENTATION DETAILS

E.1 HYPERPARAMETERS

This section provides details about the pretraining and fine-tuning of LSM and other baseline methods. The pretraining hyperparameters, detailed in Table 15, were chosen with hyperparameter sweeps. In Table 16, we include hyperparameters for linear probe and fine-tuning. The hyperparameters for supervised baseline training are detailed in Table 17. Note that hyperparameters used for the few-shot experiments found in Table 11 are similar to those found in Tables 16 and 17 with slight changes in learning rate.

E.2 TRAINING AUGMENTATIONS

Traditional image augmentations are not always valid when applied to sensor-images. For example, random crop and resize, often applied in contrastive pretraining are invalid for sensor images, as a random crop may remove a subset of senor signals. Thus, we define a subset of augmentations valid for sensor-images. These are random *Flip*: a flip along the temporal axis; *Stretch*: a stretch along the temporal axis of and subsequent crop of back to original time length; and *Noise*: the addition of Gaussian noise.

E.3 DISCRIMINATIVE TASK TUNING AND EVALUATION

In an effort to mitigate confusion regarding the implementation of our downstream discriminative tasks we cover possible questions and implementation details. All discriminative tasks operate on 5-hour wearable sensor feeds, the same form of input used during pre-training. These windowed samples are associated with metadata including a person's biological sex, age, and any activity events occurring during the 5 hour span. Activity labels are self-reported and with the corresponding events varying in duration (e.g., a bike ride may last several hours, whereas a HIIT workout may only last 30 minutes). Generally, these events are self-reported post hoc. As activity events are self-reported it is possible that other unreported events may also exist in the 5 hour span. As we discuss in Appendix C.3, this may result in degraded performance.

Table 15: **Hyperparameters for pretraining** with MAE (He et al., 2022), MSN (Assran et al., 2022), DINO (Caron et al., 2021) and SimCLR (Chen et al., 2020). A solitary row value indicates that the value was used for all methods.

Configuration	LSM MAE	MSN	DINO	SimCLR
Training Steps	50000			
Warmup Steps	2500			
Optimizer	AdamW (Loshchilov, 2017)			
Opt. momentum $[\beta_1, \beta_2]$	[0.9, 0.95]	[0.9, 0.99]	[0.9, 0.99]	[0.9, 0.99]
Base learning rate	0.005	0.001	0.004	0.001
Batch size	4096			
Weight decay	0.0001			
Gradient clipping	1.0	3.0	3.0	3.0
Dropout	0.0			
Learning rate schedule	Linear Warmup & Cosine Decay			
Loss Function	Mean Squared Error			
Data resolution	26 (signal)$\times$300(minute)			
Augmentation	Flip, Stretch, Noise			

Table 16: **Hyperparameters for LSM Linear Probing and Fine-Tuning on Discriminative Tasks** detailed in Section 4.2. A solitary row value indicates that it was used for all methods. LP=Linear Probe. FT=Fine-Tune (full model).

Task	Exercise Detection		Activity Recognition		Sex Classification		Age Classification		Mood Recognition	
Configuration	LP	FT	LP	FT	LP	FT	LP	FT	LP	FT
Training Steps	400	400	300	300	300	300	300	300	300	300
Warmup Step Percent	20	20	15	15	15	15	15	15	15	15
Optimizer	AdamW (Loshchilov, 2017)									
Opt. momentum $[\beta_1, \beta_2]$	[0.9, 0.95]									
Base learning rate	0.5	0.00005	0.5	0.00005	0.05	0.0005	0.05	0.00005	0.005	0.005
Batch size	128	128	128	128	128	128	256	256	256	256
Weight decay	0.0001									
Gradient clipping	1.0									
Dropout	0.3	0.3	0.3	0.3	0.1	0.3	0.1	0.1	0.7	0.1
Learning rate schedule	Linear Warmup & Cosine Decay									
Loss Function	Balanced Softmax Loss (Ren et al., 2020)									
Data resolution	26 (signal)$\times$300(minute)									
Augmentation	Noise									

Table 17: **Hyperparameters for Supervised Training on Discriminative Tasks** A solitary row value indicates that it was used for all methods.

Configuration	Exercise Detection	Activity Recognition	Sex Classification	Age Classification	Mood Recognition
Training Steps	400	300	300	300	300
Warmup Steps	20	15	15	15	15
Optimizer	AdamW (Loshchilov, 2017)				
Opt. momentum $[\beta_1, \beta_2]$	[0.9, 0.95]				
Base learning rate	0.0001	0.0005	0.005	0.0001	0.00005
Batch size	128	128	128	256	256
Weight decay	0.0001				
Gradient clipping	1.0				
Dropout	0.0				
Learning rate schedule	Linear Warmup & Cosine Decay				
Loss Function	Balanced Softmax Loss (Ren et al., 2020)				
Data resolution	26 (signal)$\times$300(minute)				
Augmentation	Noise				

F Description of Pretraining and Baseline Methods

F.1 Pretraining Methods

There are two main approaches to pretraining, one based on contrastive learning and the other based on the reconstruction or prediction of input features. At a high-level contrastive methods where representations are learned for different views of the same training example (*positives*), and dissimilar embeddings for different training examples (*negatives*). However, there are challenges or drawbacks to this approach. First, in the sensor domain it can be non-trivial to create augmentations that do not alter the meaning (label) of the sample. For example, does stretching data for someone *running* mean that it more closely resembles the data when they *walk*? Second, generative capabilities are attractive as imputing missing data and forecasting signals into the future are useful in and or themselves. As such, purely contrastive set-up has limitations and a pretraining task based on the reconstruction of masked input tokens is attractive. A masked autoencoder is one example of such an approach that is effective at scalable learning of representations (He et al., 2022). Below we describe the pretraining methods used for LSM and our baselines.

Masked Auto Encoder (MAE) (He et al., 2022). MAE is a self-supervised learning method where the input data is randomly masked, and the model is trained to reconstruct the missing parts. It operates on the principle that forcing the model to predict missing information helps it learn meaningful representations. MAE has shown strong performance in various vision and signal tasks, particularly in cases where large-scale unlabeled data is available.

SimCLR (Chen et al., 2020). SimCLR is a contrastive learning framework that learns representations by maximizing agreement between different augmented views of the same data sample. The method uses a contrastive loss, which encourages the model to pull together similar views of the same sample while pushing apart views of different samples. SimCLR has been widely used in both vision and sensor data for representation learning without requiring labeled data.

Masked Siamese Network (MSN) (Assran et al., 2022). MSN combines the benefits of invariance-based pretraining with mask denoising. MSN operates by matching the representation of an image view with randomly masked patches to the representation of the corresponding unmasked image. This pretraining strategy leverages Vision Transformers by processing only the unmasked patches, significantly enhancing scalability. The framework enables the generation of semantically rich representations, which perform competitively in low-shot image classification tasks.

DINO (Caron et al., 2021). DINO is a self-distillation method that trains the model using knowledge distillation, without the need for labeled data. It leverages a teacher-student network architecture, where the teacher generates target representations for the student to learn from. DINO has demonstrated success in generating robust representations that can be transferred to various downstream tasks.

F.2 Generative Baselines

We define a number of baselines for our generative tasks. Similar methods are common-place in the image domain (often used for up-sampling) (Han, 2013), and the Internet of Things (IoT) sensor domain (often for imputing corrupted and/or missing data) (Adhikari et al., 2022).

Mean Fill. Mean Fill is a simple baseline for generative tasks, where the missing values for a sensor stream are replaced by the mean value of the sensor data present in a given sample. Though naive, this method provides a reasonable estimate in certain contexts where missing values are randomly distributed.

Nearest Neighbor Fill. Nearest Neighbor Fill imputes missing data by using the value of the nearest observed neighbor for a given feature along the temporal axis. In the absence of a past and future neighbors this method mirrors back/forward fill. This method works well when there is a high degree of local similarity in the data.

Linear Interpolation. Linear Interpolation fills missing values by interpolating linearly between known values along the temporal dimension. In the absence of a past and future neighbors this method mirrors back/forward fill. This baseline is often used in time-series and spatial data, where the assumption is that changes between data points occur in a smooth, continuous manner.

Multivariate Imputation by Chained Equations (MICE) (Van Buuren & Groothuis-Oudshoorn, 2011). MICE is an imputation technique which builds a regression model, per feature, conditional upon all observed data across all variables. The method iterates through feature variables and imputes missing data. This iteration process is run multiple times with the imputation being refined each iteration. It should be noted that MICE performs best when missingness is random (Azur et al., 2011) and may under-perform in situations of large or structured missing data.

For all generative baseline methods, in the rare cases where the sensor feature is completely missing, the feature values are replaced with zeros. This remains a valid strategy as all features are z-score normalized and centered around zero.

F.3 Classification Baselines

Vision Transformer (ViT) (Dosovitskiy, 2020). The Vision Transformer (ViT) is a transformer-based architecture that treats image patches or signal segments as input tokens, similar to how transformers handle sequences in natural language processing. ViT has shown competitive performance across various classification tasks, especially when trained with large amounts of data, and serves as a strong baseline in both vision and sensor classification tasks.

Random Forest (Breiman, 2001). Random forest is a statistical machine learning method. This ensemble method fits multiple decision trees to various splits of a dataset. When applied to a classification task, the random forest uses a majority voting scheme across the decision trees to classify the sample.

Logistic Regression Classifier. A logistic regression model applies the sigmoid function to a linear combination of input variables to predict some output value. In the case of a N multi-class classification problem N logistic regression models are created, each modeling binary classification of a single class. The resulting N model probability scores are compared with the highest score dictating the predicted class.

G Additional Details of Dataset

G.1 Dataset Details

In Table 18 we detail the 26 derived sensor signal features leveraged by our methods.

G.2 Practical Constraints of Data Collection

As mentioned earlier in Section 3.1, we use 1-minute granularity features due to practical constraints. Specifically these features are aggregated at the minute level and saved on-device at a

minute granularity. The exception is heart rate which is calculated per second. This is to reduce the battery and memory burden of writing and saving raw features. Further more, streaming data from the wearable device presents another practical constraints, and the use of aggregated features allows easier transfer of this data.

G.3 Sampling of Event Classes

Event labels, for tasks like activity and mood recognition, do not occur naturally balanced. For this reason, we sub-sample event data to generate more balanced task-specific datasets. For example almost 90% of logged activities are walking, and thus activities are sampled to increase the relative proportion of under-represented classes (e.g. elliptical, and weightlifting). The natural distribution of these events along with our sample distributions can be found in Table 19.

G.4 The Utility of Minutely Features

Raw sensors are generally sampled at much higher rate than our minutely features. Through this compression it is likely that we lose features vital in capturing higher frequency activities. For this reason it is important to ground the utility of our minutely features and their ability to discriminate different life events. To this end we add a qualitative example of minutely wearable data across different activities aggregated across samples. Fig. 14 indicates that there are differences (albeit subtle) for activities at the minutely resolution.

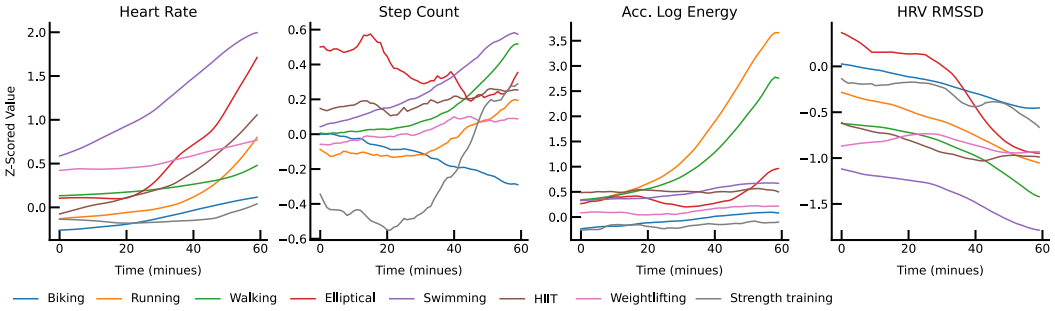

Figure 14: **Average Features by Activity Class.** Average (i) Heart Rate, (ii) Step Count, (iii) Accelerometer Log Energy and (iv) HRV RMSSD for each of the activity classes.

H Broader Impact

Wearable sensors have been shown to have a positive effect on health and well-being, promoting physical activity, sleep and have potential to surface unseen or unperceived actionable health information. Foundation models increase the potential value of these data for the above applications and hold promise for enabling new insights and opportunities to improve health.

We support open science principles and the value of open data for scientific research; however, we have to balance these considerations with the privacy of the participants and protection of their health data. Although the training data could be de-identified, some of the data streams could not be fully anonymized. We recognize that the inability to share data of this kind is a limitation; however we believe that the results enable us to share valuable insights to the community.

Meanwhile, `LSM` serves as the stepping stone towards generating large-scale, realistic synthetic datasets. These synthetic data could mimic real-world sensor patterns without compromising participant privacy and offer a promising resource for cross-institutional research collaboration. By facilitating data sharing in this way, we can overcome the current limitations in data availability and unlock new opportunities for collaborative insights and advancements for the community.

Table 18: **Sensor Feature Definitions.** Names, units and definitions of the 26 Accelerometer, PPG, skin conductance and altimeter features we use.

Feature	Unit	Definition
SCL **Skin Conductance**		
Skin Conductance Value	μSiemens	Center of linear tonic SCL value fit.
Skin Conductance Slope	μS/Min	Intraminute slope of SCL values.
TMP **Skin Temperature**		
Skin Temperature Value	$^{\circ}$C	Mean skin temperature.
PPG **Photoplethysmography**		
Heart Rate	Beats/Min	Mean of instantaneous heart rate.
RR Percent Valid	%	% of 5-minute window with valid RR intervals.
RR 80th Percentile	Msec	80th percentile of 5-minute window of RR ints.
RR 20th Percentile	Msec	20th percentile of RR ints.
RR Median	Msec	Median RR interval.
RR Mean	Msec	Mean RR interval.
Shannon Ent. RR	Nats	Shannon entropy of the RR intervals.**
Shannon Ent. RR Diffs	Nats	Shannon entropy of the RR interval differences.**
PNN30	%	% of successive RR ints. that change by $>$ 30ms.
RMSSD	Msec	Root mean squared st. dev. of RR ints.
SDNN	Msec	Standard deviation of RR intervals.
On Wrist	Boolean	If optical-sensor off-wrist within a 30-second window, then false.
ACC **Accelerometer**		
Jerk Autocorrelation Ratio	a.u.	Ratio of lag=1 autocorrelation to energy in 1st 3-axis principal component.
Step Count	Steps	Number of steps.
Log Energy	a.u.	Log of sum of 3-axis root mean squared magnitude.
Covariance Condition	a.u.	Estimate of condition number for 3-axis covariance matrix.
Log Energy Ratio	a.u.	Log of ratio of sum of energy in 1st 3-axis principal component over energy of 3-axis root mean squared magnitude.
Zero Crossing St.Dev.	Seconds	Standard deviation of time between zero crossing of 1st 3-axis principal component.
Zero Crossing Average	Seconds	Mean of time between zero crossing of 1st 3-axis principal component.
Robust Arm-Tilt	a.u.	Log of mean square root of squared X & Z axes.
Kurtosis	a.u.	Kurtosis of 3-axis root mean squared magnitude.
Sleep Coefficient	a.u.	Sum of 3-axis max-min range, binned into 16 log-scaled bins.
ALT **Altimeter**		
Altimeter St.Dev. Norm	Hectopascals	Standard deviation of altimeter readings.

I CODE ACKNOWLEDGEMENTS

We build our methods upon the *Scenic* project (Dehghani et al., 2022), an open source codebase for vision tasks implemented in JAX with Flax. *Scenic* provides rich infrastructure for attention-base vision models and common vision baselines. The project page can be found here: github.com/google-research/scenic.

Table 19: **Details of Natural and Sampled Event Datasets.** Summary of class distributions (as a percent of total task events) for activity and mood datasets.

Task	Class	Natural Distribution	Sampled Distribution	
			Train	Test
Activity	Biking	2.54%	8.73%	13.1%
	Elliptical	0.02%	1.11%	1.56%
	High Intensity Training	0.22%	2.44%	3.31%
	Strength Training	0.24%	1.68%	13.52%
	Swimming	1.41%	17.08%	14.02%
	Running	6.65%	13.62%	10.01%
	Walking	88.59%	50.44%	41.36%
	Weightlifting	0.33%	4.90%	3.11%
Mood	Content	29.71%	22.13%	20.62%
	Frustrated	11.65%	12.95%	17.24%
	Excited	5.52%	11.48%	10.23%
	Calm	31.73%	21.58%	22.96%
	Stressed	21.39%	31.86%	28.95%